Chemosphere 308 (2022) 136352

Contents lists available at ScienceDirect

Chemosphere

journal homepage: www.elsevier.com/locate/chemosphere

Different degradation mechanisms of low-concentration ozone for MIL-100 (Fe) and MIL-100(Mn) over wide humidity fluctuation

Guanqing Song [a,b], Gansheng Shi [a], Lu Chen [a], Xiao Wang [a], Jing Sun [a], Lei Yu [c,**], Xiaofeng Xie [a,*]

[a] State Key Lab of High Performance Ceramics and Superfine Microstructure, Shanghai Institute of Ceramics, Chinese Academy of Sciences, 1295 Dingxi Road, Shanghai, 200050, China
[b] University of Chinese Academy of Sciences, 19 (A) Yuquan Road, Beijing, 100049, China
[c] Shandong University of Science and Technology, 17 Shenglizhuang Road, Jinan, 250031, China

HIGHLIGHTS

- Degradation mechanisms of ozone for MIL-100(Fe) and MIL-100(Mn) were developed.
- Oxygen vacancy played a leading role in normal temperature catalysis.
- Photogenerated e^- acted as the dominant active species during photocatalysis.
- Lewis acid sites was the critical factor in the ozone removal of high humidity.

GRAPHICAL ABSTRACT

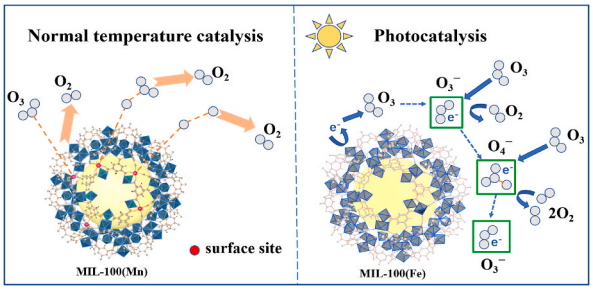

ARTICLE INFO

Handling Editor: Volker Matthias

Keywords:
Ozone
MIL-100
Photocatalytic
Normal temperature catalytic
Humidity

ABSTRACT

The synergistic control of ozone and fine particulate matter is a research hotspot in the current environmental fields. Among the ozone removal, wide humidity fluctuation and low concentration dynamic adsorption are two thorny problems. In this work, MIL-100(Fe) and MIL-100(Mn), synthesized by hydrothermal and solvothermal methods respectively, were selected to investigate the degradation of flowing ozone pollutants. The samples showed different ozone degradation mechanisms, namely photocatalytic degradation and normal temperature degradation. Notably, MIL-100(Fe) exhibited more outstanding photocatalytic activity than MIL-100(Mn), while the normal temperature catalytic efficiency of MIL-100(Mn) was much superior to MIL-100(Fe). For different humidity conditions, MIL-100(Fe) has the optimal photocatalytic performance at 10% humidity, which is 38%, while MIL-100(Mn) has basically no change in normal temperature catalytic degradation efficiency at different humidity levels of 10–90%. Furthermore, the degradation mechanism was proposed by in-situ DRIFTS and ESR, which was significantly correlated with oxygen vacancy and photogenerated electron efficiency. By the aid of Temperature Programmed Desorption (TPD), a large quantity of Lewis acid sites was detected in MIL-100(Mn), which was the critical factor that the selected materials could maintain excellent normal temperature degradation performance under high humidity. This work will expand the practical application of ozone removal and improve the degradation efficiency.

* Corresponding author.
** Corresponding author.
E-mail addresses: skd992512@sdust.edu.cn (L. Yu), xxfshcn@163.com (X. Xie).

https://doi.org/10.1016/j.chemosphere.2022.136352
Received 13 June 2022; Received in revised form 22 August 2022; Accepted 2 September 2022
Available online 8 September 2022

1. Introduction

The ozonosphere is very important to human life because it can protect human beings from excessive ultraviolet radiation. However, ground ozone may cause harm to human health when the ozone concentration exceeds the legal standard (The two faces of ozone, 2020). The World Health Organization (WHO) pointed out that the maximum ozone concentration of the working environment was limited to 100 ppb. Otherwise, it will be harmful to individuals' hearts, lungs, and respiratory tracts (Neidell, 2009).

Normal temperature catalytic technology was widely used for ozone removal because it has the advantages of being carried out under ambient temperature, low energy consumption, and high degradation efficiency (Namdari et al., 2021). Previous studies on normal temperature catalytic degradation of ozone mainly focused on high concentration ozone (>20 ppm) and fixed bed model, which were mainly used in the fields where the exhaust emission seriously exceeded the standard, such as water treatment and medical field (Li et al., 2020). Nevertheless, the actual ozone concentration of the atmosphere and indoors is low, which is generally in the condition of ppb concentration and flow phase reaction system. The reports on low-concentration ozone degradation were rare in the past, which might be attributed to the fact that low concentrations of ozone are more difficult to be captured and degraded (Ren et al., 2014). In addition, another arduous challenge for ozone reduction is humidity, most catalysts will be inactivated in high humidity, such as MnO_2(Liu et al., 2018), MnO_x/Al_2O_3(Chen et al., 2018), and CuO(Spasova et al., 2007). A novel catalyst with γ-like MnO_2 was reported by Xu et al. (2021) to investigate the catalytic decomposition of ozone, which showed that a great number of oxygen vacancies induced by the unique structure of the γ-like MnO_2 accelerated ozone removal under moist conditions. Zhang et al. (2022) showed that a series of spinel $(Mn,Co)_3O_4$, which obtained high ozone degradation performance by accelerating the conversion of peroxide species (O_2^{2-}).

It is noteworthy that excessive concentrations of ozone occurred mostly in summer when the sunlight is strong. Therefore, photocatalysis is also a sensible method for ozone elimination. Compared with normal temperature catalysis, photocatalysis adds a light source as a reaction condition, and there is no significant temperature difference of the two reactions. In practical applications, photocatalysis can be used as a supplementary means of normal temperature catalysis, making full use of natural sunlight to further degrade ozone. Agustin R et al. (Gonzalezelipe et al., 1981) revealed the photocatalytic mechanism of ozone decomposition for the first time, opening a new direction of ozone removal. Julia Patzsch et al. (Patzsch and Bloh, 2018) reported a strategy that the transition metal and titanium dioxide were combined as a photocatalyst, which boosted charge separation and electron transfer kinetics. Actually, photocatalytic technology has not been investigated extensively on ozone abatement in the past decades. Especially, exploration of reports on the simultaneous degradation of ozone by normal temperature catalysis and photocatalysis has not been covered yet. Given all of that, it is urgent to exploit a new catalyst that can solve the above-mentioned issues in terms of ozone decomposition.

Considering the high specific surface area and adjustable pore size, Metal-organic frameworks (MOFs) were widely used in catalytic removal of harmful gases (Kitagawa and Matsuda, 2007). MIL-100(Fe) had demonstrated great potential in ozone degradation due to its humidity stability (Jeremias et al., 2012). Wang et al. (2018) introduced MIL-100(Fe) into ozone degradation, which provided a novel choice for ozone decomposition. In our previous study (Chen et al., 2022), MIL-100 (Fe) was tested for BTXS′ elimination to prove its positive photocatalytic performance. Apart from these, Mn has been most frequently studied for eliminating ozone because of its' flexible valence change (Tatibouet et al., 2019). Zang et al. (Sun et al., 2021) tried to use a Manganese-Organic Framework (ZZU-281) to remove ozone and achieved a satisfactory outcome. Given the above findings, MIL-100(Mn) presumably has an advantage on ozone removal.

In this work, MIL-100(Fe) and MIL-100(Mn) were selected to simulate the degradation of ozone in the atmosphere, which introduced normal temperature catalysis and photocatalysis. Under three humidity conditions (RH = 10%, 50%, and 90%), both materials played a beneficial role in ozone removal, while the mechanisms were quite different. MIL-100(Mn) had a good effect on normal temperature catalytic degradation of ozone, while the photocatalytic efficiency was inadequate. On the contrary, MIL-100(Fe) performed badly in the normal temperature catalytic reaction, while it had a significant advantage over the photocatalytic stage. A series of physicochemical methods were conducted to reveal the various performance of these two materials. ESR revealed abundant oxygen vacancies were important for normal temperature catalysis. Photo-current response and Photoluminescence spectra (PL) showed that the high efficiency of photogenerated electrons greatly accelerated the photocatalytic degradation of ozone.

2. Experimental

2.1. Chemicals

Trimesic Acid (99%+), Manganese (II) Nitrate Tetrahydrate ($Mn(NO_3)_2{\cdot}4H_2O$) and Iron nitrate nonahydrate ($Fe(NO_3)_3{\cdot}9H_2O$) were obtained from Shanghai Titan Scientific Co., Ltd. Ethanol and methanol were purchased from Shanghai Zhenxing Co., Ltd, and Shanghai Lingfeng chemical reagent Co., Ltd, respectively. The materials mentioned above were used without any prior purification.

2.2. Preparation of samples

The sample MIL-100(Mn) was synthesized by a modified solvothermal method (Reinsch and Stock, 2013). Firstly, 5 mmol $Mn(NO_3)_2{\cdot}4H_2O$ and 5 mmol H_3BTC were melted into 30 mL methanol at the stirring speed of 300 r/min for 40 min. Subsequently, the as-prepared mixed liquid was transferred to an autoclave (100 mL) and maintained at 125 °C for 10 h. The crude product was obtained by centrifugation, and the final product was acquired via vacuum drying. MIL-100(Fe) was prepared through a modified hydrothermal method (He et al., 2019) (Scheme S (1)), 4 mmol $Fe(NO_3)_3{\cdot}9H_2O$ and 4 mmol H_3BTC were uniformly dissolved into 30 mL deionized water, next the sample was obtained by hydrothermal heating at 125 °C for 8 h.

2.3. Characterization

By the aid of X-ray diffraction (XRD) equipped with monochromatized Cu Kα radiation (k = 1.5418 Å), we got the PXRD patterns of the samples (2theta degree of 3°-85°). Samples' SEM images were obtained from field-emission scanning electron microscopy (Hitachi SU8220). The Infrared spectrum was carried on the Bruker Vertex-70 FTIR. Cary 5000 UV–Vis–NIR was conducted to analyze samples' UV–vis absorption spectra. By dint of Phase Change Temperature Analyzer (PCA-1200), the NH_3-TPD pattern was obtained. The photoluminescence (PL) spectroscopy was tested on a PerkinElmer Inc. - LS 55 Luminescence Spectrometer with the wavelength of 420 nm. The transient photocurrent experiment was undertaken by a CHI660D photoelectrochemical workstation equipped with a three-electrode system. The degradation curve of ozone was collected by an ozone Analyzer (Model 49i, U.S.A. EPA). Samples for ESR measurements were used to detect oxygen vacancy by a JES-FA200 spectrometer.

2.4. Catalytic activity

By the customized system as shown in Fig. S1, experimental curves of the prepared materials were acquired. The reaction chamber is made of acrylic (40 × 25 × 25 cm), and a 21 W (±1) ultraviolet lamp was placed 15 cm next to the sample as the light source. The concentration of ozone flow was directly controlled by the oxygen intake and ozone generator,

which could be monitored by the ozone analyzer and four flowmeters. Due to the influence of the lamp life of the ozone generator, there might be some differences in inlet gas concentration. As for this work, the exact ozone concentration was set from 225–625 ppb. Initially, a glass plate (20 × 20 cm) with the sample (0.05 g) was prepared before the reaction (There was a gap between the glass plate and the box), and then the ozone prepared at the front slowly passed through the reactor for 6 h under dark conditions to investigate the catalytic activity of the sample. Afterwards, turn on the light for 6 h to further judge the photocatalytic degradation of ozone.

3. Results and discussion

3.1. Characterization of catalysts

The PXRD patterns of materials were displayed in Fig. 1(a). Both samples showed a characteristic peak of MIL-100 (2θ range of 3–30°), which was in agreement with the former studies (Reinsch and Stock, 2013; Zorainy et al., 2021), confirming the successful synthesis of MIL-100(Fe) and MIL-100(Mn). Moreover, it was easy to find the crystallinity of MIL-100(Mn) was higher than MIL-100(Fe). According to J. W. Yoon's study (Yoon et al., 2010), high hydrothermal temperature (160 °C) will accelerate the nucleation rate and then improve the crystallinity of MIL-100(Fe), while the MIL-100(Mn) can get high crystallinity at lower synthesis temperature (125 °C).

As shown from Fig. 1(b), the infrared spectrum curved lines of the as-prepared materials were very similar, corresponding to the unique combination of MIL-100. Take MIL-100(Mn) as an example, the band at 490 cm^{-1} could be associated with the mark of the Mn–O bond (Xu et al., 2021). The signal of 718 cm^{-1} was related to benzene ring substitution of ligand (Reinsch and Stock, 2013). As for the band at 1369 and 1621 cm^{-1}, which could be involved with the C–O stretching of BTC anions (Ha et al., 2018). And the peak of 1570 cm^{-1} was caused by the C=C stretching of benzene (Zhang et al., 2016a). As for MIL-100(Fe), the signal at 468 cm^{-1} should be corresponded to the characteristic signal of the Fe–O bond, which showed a slight red shift compared with the Mn–O bond. In light of Christian Tantardini's work (Tantardini and Oganov, 2021), this might be related to the lower electronegativity of iron. The slight shift of other bonds, such as 718 cm^{-1}, might be owing to different metal elements and coordination environments (Morris and Brammer, 2017).

Fig. 2 showed the micro-morphology of as-prepared materials. MIL-100(Fe) presented an elliptical granular ball, while the main structure of the MIL-100(Mn) exhibited crossed meshes. Both materials had uneven surfaces and some defects, which might be beneficial to the capture and reaction of ozone molecules (Gao et al., 2021).

3.2. Photocatalytic activity of catalysts

The corresponding optical range and band gap of materials are two of the important factors to characterize their photocatalytic performances (Liu et al., 2017). From Fig. 3(a), both samples presented two main absorption peaks. The peak of 300 nm was connected to the absorption of ligand-to-metal charge transfer (LMCT) (Bordiga et al., 2004). Furthermore, the band at the range of 450–500 nm should be related with the reaction [$^6A_{1g} \rightarrow {}^4A_{1g} + {}^4Eg(G)$], which was caused by Fe^{3+} or Mn^{3+} of MIL-100 (Blake and Yavari, 1982). With the purpose of understanding its band gap, we prepared the converted Kubelka–Munk function curve. As shown in Fig. 3(b), the optical band gap of MIL-100 (Fe) and MIL-100(Mn) were 2.09 eV and 1.77 eV respectively, which showed that MIL-100(Mn) had a larger light absorption range.

3.3. Degradation performance of ozone

We preliminarily determined the optimum catalyst loading by adjusting the amount of sample with 20, 50 and 100 mg, respectively (Fig. S2). It could be easily seen from the image that 50 mg was the best choice, so the following experiments were carried out with 50 mg samples. Humidity has been recognized as a knotty problem in ozone degradation, so we designed all humidity range experiments. The degradation curves of ozone under different humidity of samples were demonstrated in Fig. 4(a), (b) and (c). The first 6 h were the normal temperature catalytic stage, the air passed through the humidifier and mixed with ozone in the gas-mixed jar, and then entered the reaction chamber at a flow rate of 700 mL min^{-1}. As for the next 6 h, the photocatalytic activity was estimated under the 21 W ultraviolet lamp. Based on the experiment results, it was not difficult to conclude that the two samples played divergent roles in the trial runs. Most specifically, MIL-100(Fe) has advantages on ozone degradation in the normal temperature catalysis, while the photocatalytic efficiency was not very satisfactory. On the other hand, MIL-100(Mn) showed a fine performance in the normal catalytic stage, but not for photocatalysis.

In the matter of the influence of water, Fig. 4(d) displayed the degradation efficiency of the samples under different humidity. For MIL-100(Fe), with increasing RH from 10% to 50%, the normal catalytic efficiency went from 8% to 12%. Water molecules were able to bind to the exposed metal centers to form Fe^{III}-bound water in MIL-100(Fe) (Wang et al., 2018). The pKa of Fe^{III}-bound water decreased rapidly with the increase of water molecule adsorption, which was conducive to the deprotonation of trivalent iron to form MIL-100(Fe) hydroxide. The hydroxide was profitable to the adsorption and degradation of O_3. When the humidity increased to 90% RH, the degradation efficiency decreased by 2% compared with 50% RH. This was probably because excessive adsorbed water molecules could occupy part of the active sites on the sample, developing a competitive relationship with the adsorption of ozone. In terms of the photocatalytic process, the value of removal rate showed a downward trend with the increase of humidity, this was largely owing to the fact that water molecules were detrimental to the combination of O_3 and photo-generated electrons (Lu et al., 2014). Interestingly, the maximum removal efficiency of MIL-100(Mn) was monitored at 90% RH. Thomas et al. (Mathew et al., 2011) used density functional calculations (DFT) to find unsaturated iron sites that can

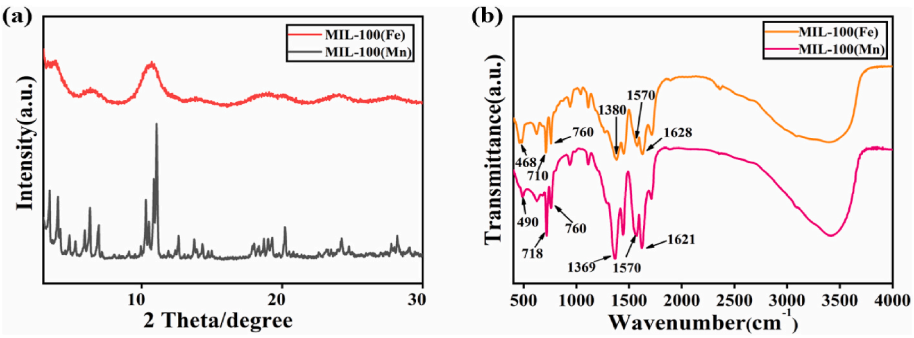

Fig. 1. (a) PXRD patterns and (b) DRIFTS spectra of MIL-100(Fe) and MIL-100(Mn).

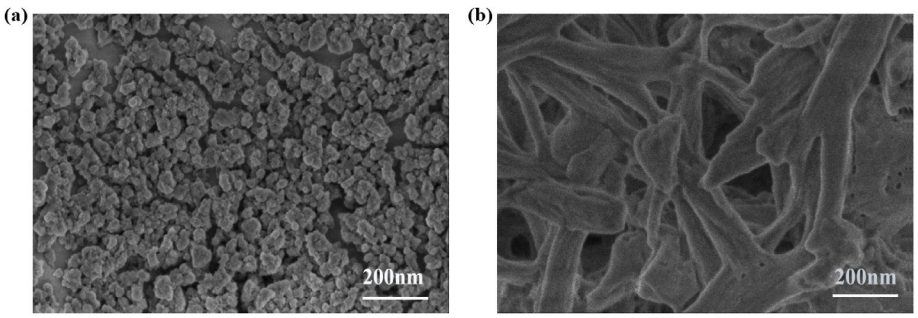

Fig. 2. Surface SEM images of (a) MIL-100(Fe) (b) MIL-100(Mn).

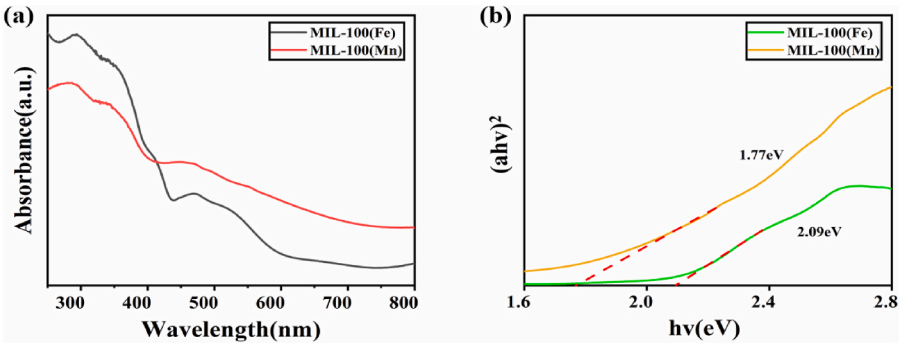

Fig. 3. (a) UV–vis spectra (b) The converted Kubelka–Munk function curve.

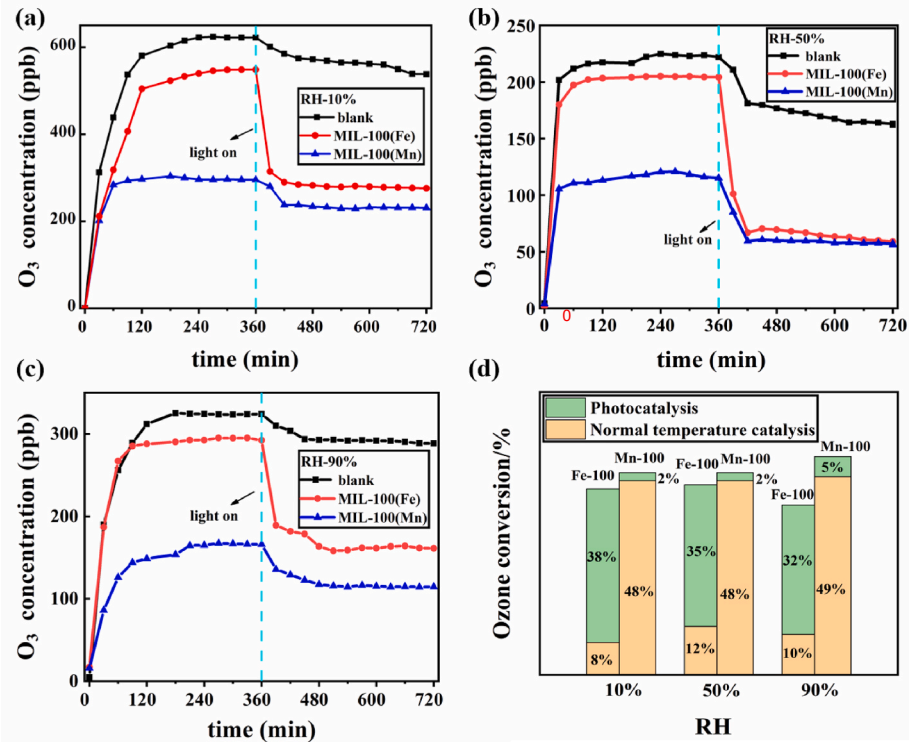

Fig. 4. Degradation plot of ozone under different humidity (a)RH-10%, (b) RH-50%, (c) RH-90%., (d)Degradation efficiency towards ozone under different humidity.

facilitate ozone decomposition by forming reactive peroxide species. Wang (Wang et al., 2018) also found the similar phenomenon, MIL-100 (Fe) could bind with water molecules to form hydroxides (i.e., Fe^{III}–OH-) by unsaturated iron sites, and the hydroxides promoted ozone degradation. Consequently, we thought the excellent performance of MIL-100(Mn) at 90% RH was due to the combination of water molecules with the unsaturated sites of manganese, and then formed some novel active species which could promote ozone elimination.

For the sake of exploring the stability of the sample, we had also conducted durability test experiments (Fig. S3). Furthermore, the sample before and after the reaction was analyzed by XRD and infrared spectroscopy (Fig. S4). The main peak had no obvious change after 72 h, which could prove the excellent stability of the sample.

3.4. The mechanism of ozone degradation

As recognized in earlier researchs, oxygen vacancy played a major part in the normal temperature catalytic stage (Hong et al., 2021). We estimated that the large difference in normal temperature catalytic efficiency between MIL-100(Fe) and MIL-100(Mn) might be led by their different contents of oxygen vacancy, and ESR test was organized to analyze the production of oxygen vanancy (Sundarapandiyan et al., 2017).

From the test results in Fig. 5, we could see that both samples had the signal at g = 2.01, which was the mark of oxygen vacancy (Zhang et al., 2016b). The results showed that the maximum value of MIL-100(Mn) was 6667, while MIL-100(Fe) was 1949. Based on the typical research (Li et al., 1998), the amount of oxygen vacancy directly determined the ability of catalytic degradation of ozone at room temperature, and the degradation of ozone was mainly carried out through the following three reactions:

$$O_3 + * \rightarrow O_2 + O* \quad (1)$$

$$O_3 + O* \rightarrow O_2 + O_2 * \quad (2)$$

$$O_2 * \rightarrow O_2 + * \quad (3)$$

In the case of the above equations, the symbol * represented surface reaction sites, and O_2* stood for the peroxide species. Referring to previous literature (Gonzalezelipe et al., 1981), photogenerated electron was quite vital for photocatalytic degradation of ozone. The main reaction process was as follows:

$$O_3 + e^- \rightarrow O_3^- \quad (4)$$

$$O_3^- + O_3 \rightarrow O_2 + O_4^- \quad (5)$$

$$O_4^- + O_3 \rightarrow 2O_2 + O_3^- \quad (6)$$

In order to confirm the scientificity of the above reactions, in-situ infrared spectra was conducted to capture the relevant active groups. The system was designed in a flow of O_3 at environmental temperature, and the infrared background peak of the sample was deducted before the reaction. As could be seen from Fig. 6, there was the normal temperature catalytic (dark) and photocatalytic stage (light) from bottom to top. It was not difficult to see, there were two main homologous bands for the above two materials: 1040–1060 cm^{-1} (gray), and 1400 cm^{-1} (yellow), which could be caused by adsorbed ozone molecules on weak Lewis acid sites (Bulanin et al., 1995) and atomic oxygen intermediate attached to strong Lewis acid sites (Roscoe and Abbatt, 2005), respectively. The appearance of the atomic oxygen signal directly demonstrated the occurrence of the above ozone degradation process.

The Lewis acid sites were tested by TPD (Fig. S5), referring to R.F. Nie's work (Nie et al., 2012), the peak at about 100 °C was the weak Lewis acid site, while the peak at 150–200 °C was a strong Lewis acid site. A large number of Lewis acid sites were not only profitable to the adsorption of O_3, but could inhibit the competition of water molecules on the active sites under high humidity (Yu et al., 2021). This was consistent with the above analysis results, which could explain that the selected materials could still maintain excellent performance under high humidity.

Building on the above discussion, we proposed the reaction mechanism of ozone degradation (Scheme 1). For the normal temperature catalytic process, the surface site was caused by the coordination unsaturated of MIL-100(Mn). The first O_3 combined with the surface site and removed O_2 to form a new active group O*, then the second ozone molecule reacted with the new group O* and released another oxygen molecule. Finally, the active group O_2 * got rid of an oxygen molecule to form a closed loop.

Aiming at the photocatalytic stage, electrons were generated from the sample under a light source, an ozone molecule absorbed an electron to form an active group O_3^-, then the next O_3 reacted with O_3^- and released O_2, leaving a group O_4^-. In the last step of the trial, O_4^- combined with another ozone molecule and released two oxygen molecules.

From the photocurrent curves (Fig. 7(a)), it was easy to find that the MIL-100(Fe) sample showed a stronger photocurrent response than MIL-100(Mn). Compared with MIL-100(Mn), the emission intensity (λ = 320 nm) for MIL-100(Fe) was much lower (Fig. 7(b)), signifying a weaker recombination probability of photogenerated electron-hole pairs. The above results were probably bound up with the narrow band gap of MIL-100(Mn), which greatly increased the recombination rate of photogenerated electron-hole (Hasan et al., 2017). Considering that the total amount of photogenerated electrons produced by MIL-100(Fe) was wider than by MIL-100(Mn), and the recombination rate of electron-hole was lower, so its photocatalytic activity was much better than MIL-100(Mn).

4. Conclusion

In summary, MIL-100(Fe) and MIL-100(Mn) were successfully synthesized by hydrothermal method and solvothermal method severally for ozone degradation. By simulating the system of low concentration and mobile phase in an atmospheric air environment, it was found that both MIL-100(Fe) and MIL-100(Mn) had a certain effect on ozone decomposition, the degradation efficiency of 0.05 g sample to 25 L ozone (225–625 ppb) was up to 50% (RH ranged from 10% to 90%), and the stability and durability of the samples were fantastic. In view of the result that MIL-100(Fe) only contains excellent photocatalytic performance, while MIL-100(Mn) only has advantages in the catalytic stage at environmental temperature. We revealed the different mechanisms of

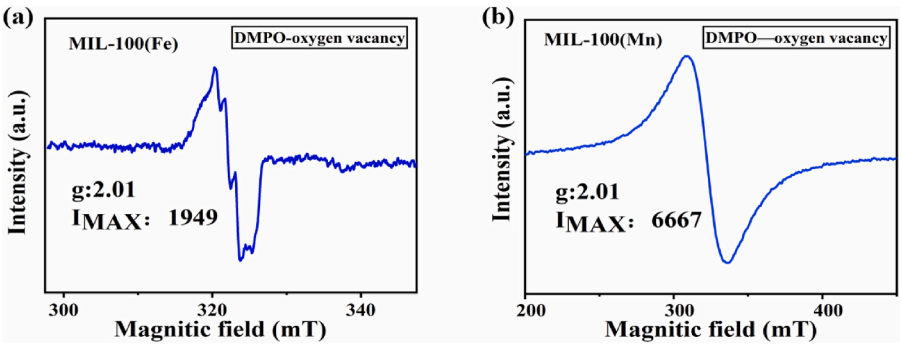

Fig. 5. ESR spectra of the oxygen vacancy (a) MIL-100(Fe) (b) MIL-100(Mn).

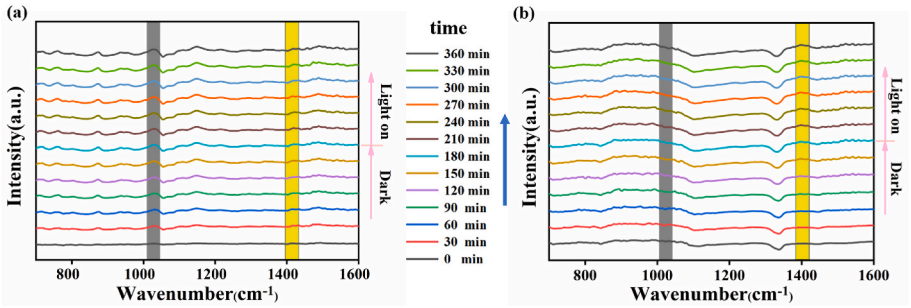

Fig. 6. DRIFT spectra of normal temperature catalysis and photocatalysis process for ozone. (a) MIL-100(Fe) (b) MIL-100(Mn).

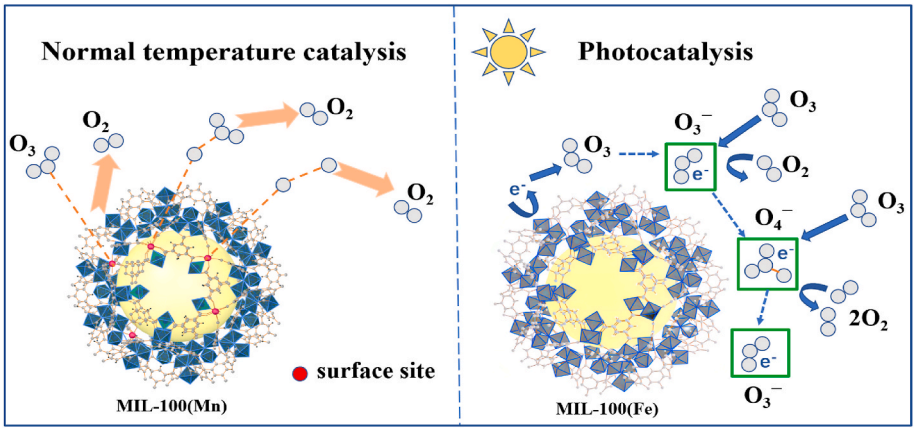

Scheme 1. Different mechanism diagrams of ozone degradation.

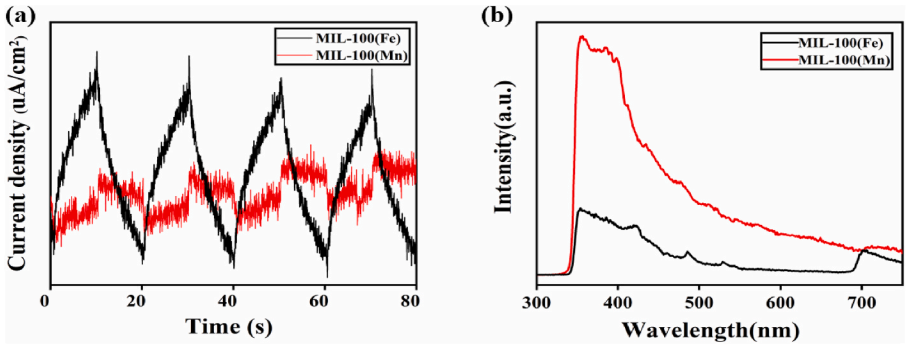

Fig. 7. (a) Photo-current response and (b) Photoluminescence spectra of MIL-100(Fe) and MIL-100(Mn).

the two materials at normal temperature catalysis and photocatalytic reaction, which were mainly owing to oxygen vacancy and photo-generated electrons. We believed that this article can provide some new ideas for the ozone degradation system and guiding significance for the design of materials eliminating ozone more efficiently.

Author contributions statement

Guanqing Song: Investigation, Validation, Data curation, Writing – original draft. **Gansheng Shi**: Methodology, Formal analysis. **Lu Chen**: Methodology, Formal analysis. **Xiao Wang**: Formal analysis, Resources. **Jing Sun**: Validation, Resources. **Lei Yu**: Conceptualization, Writing – review & editing. **Xiaofeng Xie**: Conceptualization, Funding acquisition, Project administration, Writing – review & editing.

Declaration of competing interest

The authors declare that they have no known competing financial interests or personal relationships that could have appeared to influence the work reported in this paper.

Data availability

Data will be made available on request.

Acknowledgment

This work was financially supported by the National Key Research and Development Program of China (2021YFE0110400); the National Natural Science Foundation of China (41907303, 52072387); "The Belt and Road" Alliance of International Science Organization Joint Research Project (ANSO-CR-KP-2020-13); Shanghai Commission of Science and

Technology Program (19DZ1202600, 20DZ1204100); Natural Science Foundation of Shanghai (22ZR1471800).

Appendix A. Supplementary data

Supplementary data to this article can be found online at https://doi.org/10.1016/j.chemosphere.2022.136352.

References

Blake, A.B., Yavari, A., 1982. Heterotrinuclear basic acetates containing chromium(iii), iron(iii), and a divalent metal - spectroscopic consequences of metal-metal interactions. J. Chem. Soc., Chem. Commun. 1247–1249.

Bordiga, S., Lamberti, C., Ricchiardi, G., Regli, L., Bonino, F., Damin, A., Lillerud, K.P., Bjorgen, M., Zecchina, A., 2004. Electronic and vibrational properties of a MOF-5 metal-organic framework: ZnO quantum dot behaviour. Chem. Commun. 2300–2301.

Bulanin, K.M., Lavalley, J.C., Tsyganenko, A.A., 1995. IR-Spectra of adsorbed ozone. Colloids Surf. A Physicochem. Eng. Asp. 101, 153–158.

Chen, L., Ondarts, M., Outin, J., Gonthier, Y., Gonze, E., 2018. Catalytic decomposition performance for O_3 and NO_2 in humid indoor air on a MnO_x/Al_2O_3 catalyst modified by a cost-effective chemical grafting method. J. Environ. Sci. (China) 74, 58–70.

Chen, L., Wang, X., Rao, Z.P., Tang, Z.X., Shi, G.S., Wang, Y., Lu, G.H., Xie, X.F., Chen, D. L., Sun, J., 2022. One-pot Synthesis of the MIL-100 (Fe) MOF/MOX homojunctions with tunable hierarchical pores for the photocatalytic removal of BTXS. Appl. Catal. B Environ. 303.

Gao, J., Cai, Y., Qian, X., Liu, P., Wu, H., Zhou, W., Liu, D.X., Li, L., Lin, R.B., Chen, B., 2021. A microporous hydrogen-bonded organic framework for the efficient capture and purification of propylene. Angew Chem. Int. Ed. Engl. 60, 20400–20406.

Gonzalezelipe, A.R., Soria, J., Munuera, G., 1981. Photo-decomposition of ozone on TiO_2. Zeitschrift Fur Physikalische Chemie-Wiesbaden 126, 251–257.

Ha, Y., Mu, M.M., Liu, Q.L., Ji, N., Song, C.F., Ma, D.G., 2018. Mn-MIL-100 heterogeneous catalyst for the selective oxidative cleavage of alkenes to aldehydes. Catal. Commun. 103, 51–55.

Hasan, M.T., Senger, B.J., Ryan, C., Culp, M., Gonzalez-Rodriguez, R., Coffer, J.L., Naumov, A.V., 2017. Optical band gap alteration of graphene oxide via ozone treatment. Sci. Rep. 7.

He, X., Fang, H., Gosztola, D.J., Jiang, Z., Jena, P., Wang, W.N., 2019. Mechanistic Insight into photocatalytic pathways of MIL-100(Fe)/TiO_2 composites. ACS Appl. Mater. Interfaces 11, 12516–12524.

Hong, W., Ma, J., Zhu, T., He, H., Wang, H., Sun, Y., Shen, F., Li, X., 2021. To enhance water resistance for catalytic ozone decomposition by fabricating H_2O adsorption-site in OMS-2 tunnels. Appl. Catal. B Environ. 297.

Jeremias, F., Khutia, A., Henninger, S.K., Janiak, C., 2012. MIL-100(Al, Fe) as water adsorbents for heat transformation purposes—a promising application. J. Mater. Chem. 22, 10148–10151.

Kitagawa, S., Matsuda, R., 2007. Chemistry of coordination space of porous coordination polymers. Coord. Chem. Rev. 251, 2490–2509.

Li, W., Gibbs, G.V., Oyama, S.T., 1998. Mechanism of ozone decomposition on a manganese oxide catalyst. I. In situ Raman spectroscopy and ab initio molecular orbital calculations. J. Am. Chem. Soc. 120, 9041–9046.

Li, X., Ma, J., He, H., 2020. Recent advances in catalytic decomposition of ozone. J. Environ. Sci. (China) 94, 14–31.

Liu, X.Q., Iocozzia, J., Wang, Y., Cui, X., Chen, Y.H., Zhao, S.Q., Li, Z., Lin, Z.Q., 2017. Noble metal-metal oxide nanohybrids with tailored nanostructures for efficient solar energy conversion, photocatalysis and environmental remediation. Energy Environ. Sci. 10, 402–434.

Liu, S., Ji, J., Yu, Y., Huang, H., 2018. Facile synthesis of amorphous mesoporous manganese oxides for efficient catalytic decomposition of ozone. Catal. Sci. Technol. 8, 4264–4273.

Lu, Y., Zhao, X., Wang, M., Yang, Z., Zhang, X., Yang, C., 2014. Feasibility analysis on photocatalytic removal of gaseous ozone in aircraft cabins. Build. Environ. 81, 42–50.

Mathew, T., Suzuki, K., Ikuta, Y., Nagai, Y., Takahashi, N., Shinjoh, H., 2011. Mesoporous ferrihydrite-based iron oxide nanoparticles as highly promising materials for ozone removal. Angew Chem. Int. Ed. Engl. 50, 7381–7384.

Morris, R.E., Brammer, L., 2017. Coordination change, lability and hemilability in metal-organic frameworks. Chem. Soc. Rev. 46, 5444–5462.

Namdari, M., Lee, C.-S., Haghighat, F., 2021. Active ozone removal technologies for a safe indoor environment: a comprehensive review. Build. Environ. 187.

Neidell, M., 2009. Information, avoidance behavior, and health: the effect of ozone on asthma hospitalizations. J. Hum. Resour. 44, 450–478.

Nie, R.F., Lei, H., Pan, S.Y., Wang, L.N., Fei, J.H., Hou, Z.Y., 2012. Core-shell structured CuO-ZnO@H-ZSM-5 catalysts for CO hydrogenation to dimethyl ether. Fuel 96, 419–425.

Patzsch, J., Bloh, J.Z., 2018. Improved photocatalytic ozone abatement over transition metal-grafted titanium dioxide. Catal. Today 300, 2–11.

Reinsch, H., Stock, N., 2013. Formation and characterization of Mn-MIL-100. CrystEngComm 15, 544–550.

Ren, C., Zhou, L., Shang, H., Chen, Y., 2014. Effect of preparation method on the performance of Pd-MnO_x/γ-Al_2O_3 monolithic catalysts for ground-level O_3 decomposition. Chin. J. Catal. 35, 1883–1890.

Roscoe, J.M., Abbatt, J.P.D., 2005. Diffuse reflectance FTIR study of the interaction of alumina surfaces with ozone and water vapor. J. Phys. Chem. A 109, 9028–9034.

Spasova, I., Nikolov, P., Mehandjiev, D., 2007. Ozone decomposition over alumina-supported copper, manganese and copper-manganese catalysts. Ozone: Sci. Eng. 29, 41–45.

Sun, Z.B., Si, Y.N., Zhao, S.N., Wang, Q.Y., Zang, S.Q., 2021. Ozone decomposition by a manganese-organic framework over the entire humidity range. J. Am. Chem. Soc. 143, 5150–5157.

Sundarapandiyan, S., Renitha, T.S., Sridevi, J., Saravanan, P., Chandrasekaran, B., Raju, G.B., 2017. Photocatalytic degradation of highly refractive phenolic polymer mechanistic insights as revealed by Electron Spin Resonance (ESR) and solid-state C-13 NMR spectroscopy. Chem. Eng. J. 313, 1112–1121.

Tantardini, C., Oganov, A.R., 2021. Thermochemical electronegativities of the elements (vol 12, 2087, 2021). Nat. Commun. 12.

Tatibouet, J.M., Valange, S., Touati, H., 2019. Near-ambient temperature ozone decomposition kinetics on manganese oxide-based catalysts. Appl. Catal. Gen. 569, 126–133.

The two faces of ozone. Nat. Clim. Change 10, 2020, 97, 97.

Wang, H., Rassu, P., Wang, X., Li, H., Wang, X., Wang, X., Feng, X., Yin, A., Li, P., Jin, X., Chen, S.L., Ma, X., Wang, B., 2018. An iron-containing metal-organic framework as a highly efficient catalyst for ozone decomposition. Angew Chem. Int. Ed. Engl. 57, 16416–16420.

Xu, Z., Yang, W., Si, W., Chen, J., Peng, Y., Li, J., 2021. A novel gamma-like MnO_2 catalyst for ozone decomposition in high humidity conditions. J. Hazard Mater. 420, 126641.

Yoon, J.W., Seo, Y.K., Hwang, Y.K., Chang, J.S., Leclerc, H., Wuttke, S., Bazin, P., Vimont, A., Daturi, M., Bloch, E., Llewellyn, P.L., Serre, C., Horcajada, P., Greneche, J.M., Rodrigues, A.E., Ferey, G., 2010. Controlled reducibility of a metal-organic framework with coordinatively unsaturated sites for preferential gas sorption. Angew Chem. Int. Ed. Engl. 49, 5949–5952.

Yu, D.Y., Wang, L.P., Yang, T.Y., Yang, G.P., Wang, D., Ni, H.G., Wu, M.H., 2021. Tuning Lewis acidity of iron-based metal-organic frameworks for enhanced catalytic ozonation. Chem. Eng. J. 404.

Zhang, W., Shi, Y., Li, C., Zhao, Q., Li, X., 2016a. Synthesis of bimetallic MOFs MIL-100 (Fe-Mn) as an efficient catalyst for selective catalytic reduction of NO_x with NH_3. Catal. Lett. 146, 1956–1964.

Zhang, N., Li, X.Y., Ye, H.C., Chen, S.M., Ju, H.X., Liu, D.B., Lin, Y., Ye, W., Wang, C.M., Xu, Q., Zhu, J.F., Song, L., Jiang, J., Xiong, Y.J., 2016b. Oxide defect engineering enables to couple solar energy into oxygen activation. J. Am. Chem. Soc. 138, 8928–8935.

Zhang, L., Yang, J., Wang, A., Chai, S., Guan, J., Nie, L., Fan, G., Han, N., Chen, Y., 2022. High performance ozone decomposition spinel $(Mn,Co)_3O_4$ catalyst accelerating the rate-determining step. Appl. Catal. B Environ. 303.

Zorainy, M.Y., Gar Alalm, M., Kaliaguine, S., Boffito, D.C., 2021. Revisiting the MIL-101 metal–organic framework: design, synthesis, modifications, advances, and recent applications. J. Mater. Chem. 9, 22159–22217.